Supporting Information

De and Olson 10.1073/pnas.1017442108

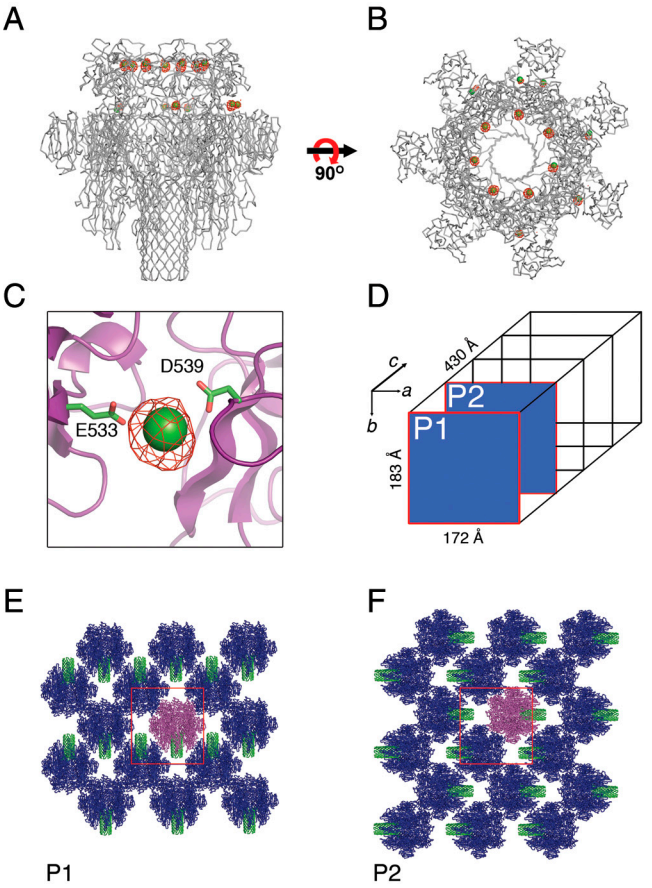

Fig. S1. Crystal phasing and packing interactions. (*A*) Side and (*B*) top views showing SHELX-located $Ta_6Br_{12}^{2+}$ sites as green spheres and anomalous difference Fourier map density in red mesh. The seven strongest sites form a symmetric ring near the top of the β-trefoil lectin domain. Maps are contoured at 5σ with peaks still visible up to approximately 15σ. (*C*) Close-up showing that tantalum clusters bind between adjacent subunits and are coordinated by negatively charged amino acids. (*D*) *Vibrio cholerae* cytolysin (VCC) oligomers pack in alternating planes (P1 and P2 shown in *E* and *F*) along the 2-fold screw axis of the *c* unit cell dimension, each containing one of two oligomers in the asymmetric unit (magenta). The transmembrane domains (green) do not participate in lattice contacts. Red boxes illustrate the *a*, *b* unit cell boundary.

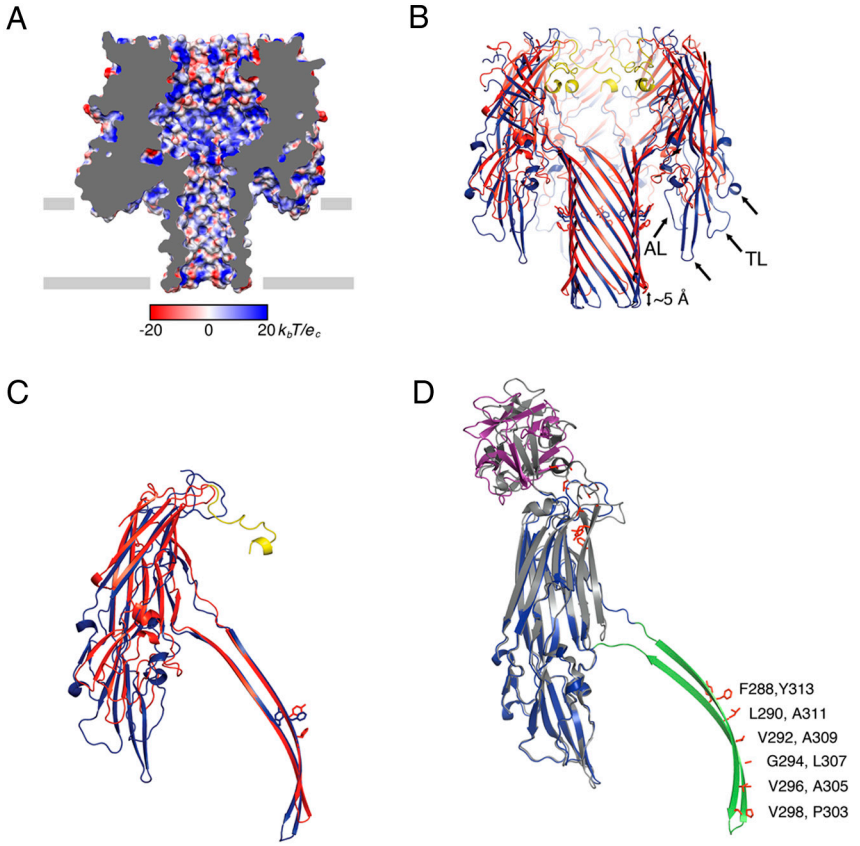

Fig. S2. Comparison of VCC and staph α-hemolysin (α-HL). (*A*) Electrostatic potential map of α-HL calculated as described in *Methods*. (*B*) Superposition of VCC (blue) and α-HL (red) sliced in half along the channel axis. The VCC stem is roughly 3–5 Å longer than the α-HL stem. Arrows point to extended loops within the VCC rim domain that may adopt a different structure (perhaps lying on top of the membrane) when the channel inserts into the membrane, and labeled to indicate putative cholesterol binding motifs (TL = T237–L238 and AL = A360–L361). (*C*) Superposition of a single protomer from VCC (blue) and α-HL (red). Aromatic residues near the membrane-solution interface are shown in stick representation (F288 and Y313 in VCC, Y118 and F120 in α-HL). The α-HL amino-latch is shown in yellow. (*D*) Superposition of the cytolytic VCC domains illustrates molecular rearrangements that occur during assembly. The water-soluble cytolysin and β-trefoil domains are shown in gray, and the assembled protomer is in blue, green, and purple. Hydrophobic residues that project into the inner leaflet of the membrane are shown in stick representation for both forms of the toxin and are mostly solvent inaccessible in the water-soluble state.

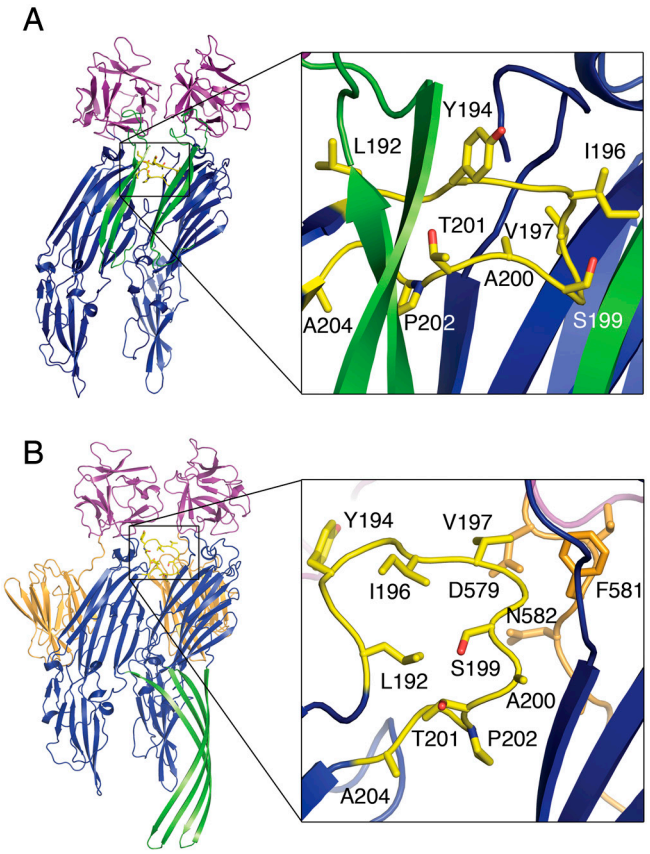

Fig. S3. Cradle loop rearrangement during assembly. (*A*) Model constructed by superimposing cytolytic and β-trefoil domains from water-soluble monomers onto adjacent protomers of the assembled VCC heptamer. The cradle loop (residues 192–204) overlaps with portions of the neighboring molecule. (*B*) Two adjacent protomers from the VCC heptamer illustrate rearranged structure of the cradle loop. The cradle loop contacts the cytolytic (blue) domain of the adjacent protomer as well as the linker between the β-trefoil and β-prism domains of the adjacent protomer (orange).

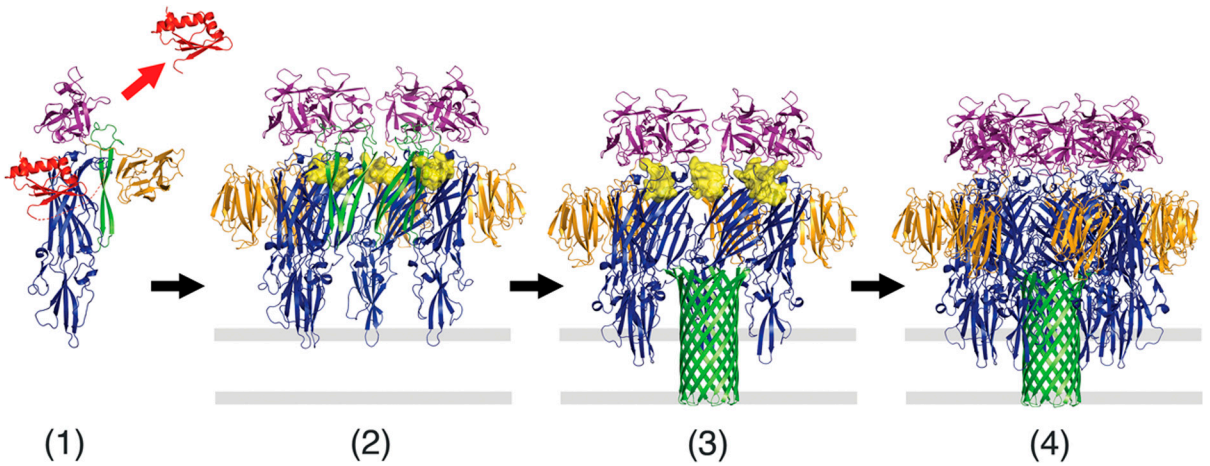

Fig. S4. Schematic model for pore-assembly. Assembly of VCC from water-soluble to membrane embedded states proceeds through a prepore state. (**1**) The proteolytic cleavage loop (dotted line) is cut by proteases activating the toxin and initiating formation of a transitional prepore state (**2**). This necessitates rearrangement of the β-prism lectin domain (gold) and release of the prodomain (red). Steric clashes involving the cradle loop (yellow space filling representation) and β-prism lectin may facilitate destabilization and unfolding (**3**) of the prepore loop (green) forming the assembled pore (**4**). Four of seven protomer subunits shown in **2** and **3** for clarity with the complete stem shown in **3**. Membrane denoted in gray.

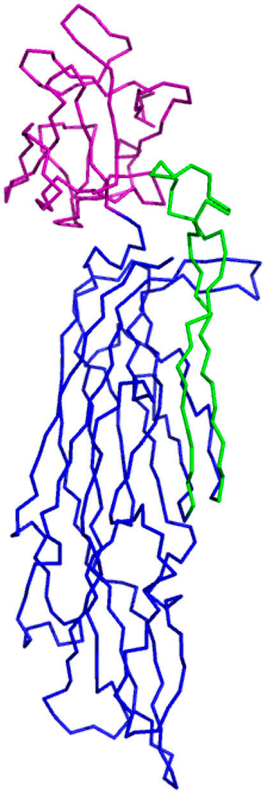

Movie S1. Morph of the VCC water-soluble monomer structure into a superimposed protomer from the assembled heptamer structure. The carboxy-terminal β-prism lectin domain has been removed for clarity. Intermediates in the assembly pathway were interpolated using the Gerstein script and CNS to minimize steric overlaps (see *Methods*).

Movie S1 (MOV)

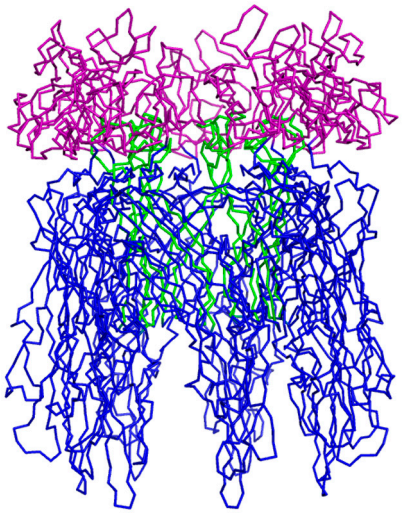

Movie S2. Morph of the prepore toxin model into the final assembled form.

Movie S2 (MOV)

Table S1. X-ray and refinement statistics

Dataset	Native (bar crystal)	$Ta_6Br_{12}^{2+}$ λ1 (inflection)	$Ta_6Br_{12}^{2+}$ λ2 (peak)	$Ta_6Br_{12}^{2+}$ λ3 (high remote)
Space group	$P2_12_12_1$	$P2_12_12_1$	$P2_12_12_1$	$P2_12_12_1$
Cell dimensions *a*, *b*, *c*; Å	172.4, 182.9, 430.4	174.0, 184.4, 432.0	173.2, 184.1, 432.0	173.4, 184.5, 432.1
Wavelength, Å	1.0000	1.2550	1.2546	1.0332
Resolution limits	86.2–2.9 (3.0–2.9)	216.0–4.0 (4.14–4.0)	216.0–4.0 (4.14–4.0)	216.0–4.0 (4.14–4.0)
Total reflections	1,362,122	696,052	697,505	869,566
Unique reflections	299,154	104,246	102,656	115,464
Redundancy	4.6 (4.3)	6.7 (3.5)	6.8 (4.3)	7.5 (7.4)
Completeness, %	98.9 (96.3)	85.5 (47.2)	86.3 (49.1)	100.0 (100.0)
R_{merge}*, %	9.6 (50.5)	22.3 (80.7)	12.7 (23.4)	22.5 (51.2)
$I/\sigma I$	14.0 (2.3)	8.3 (1.6)	13.0 (5.4)	8.6 (3.7)
Refinement statistics (model contains 62,948 atoms, 14 polypeptide chains, and 650 water molecules)				**native dataset**
Resolution limits, Å				73.9–2.9
Reflections in refinement				275,629
$R_{work}^{\dagger}/R_{free}^{\ddagger}$, %				21.8/24.9
RMSD bonds, Å				0.008
RMSD angles, °				1.053
Average *B* factor, Å^2				55.3
Ramachandran statistics				
Residues in most favored regions				96.7%
Residues in additionally allowed regions				3.3%
Residues in disallowed regions				0.0%

Numbers in parentheses denote highest resolution shell.

*$R_{merge}(I) = \sum_{hkl}|I_i - \langle I_h\rangle|/\sum_{hkl}I_i$, where I_i is the *i*th observation of the intensity of unique reflection *hkl* and $\langle I_h\rangle$ is the mean intensity of reflection *hkl*.

†$R_{work} = \sum_{hkl}||F_{obs}| - |F_{calc}||/\sum_{hkl}|F_{obs}|$, where $|F_{obs}|$ and $|F_{calc}|$ are the observed and calculated structure factor amplitudes, respectively.

‡R_{free} is the crystallographic *R* factor calculated using 5% of the data withheld from refinement.